Available online at www.sciencedirect.com
ScienceDirect
Acta Materialia 57 (2009) 3902–3915
Acta MATERIALIA
www.elsevier.com/locate/actamat

Experimental and numerical analysis of toughness anisotropy in AA2139 Al-alloy sheet

T.F. Morgeneyer [a,c,*], J. Besson [a], H. Proudhon [a], M.J. Starink [b], I. Sinclair [b]

[a] *Mines ParisTech, Centre des matériaux, CNRS UMR 7633, BP87 91003 Evry Cedex, France*
[b] *Materials Research Group, School of Engineering Sciences, University of Southampton, Southampton SO17 1BJ, UK*
[c] *Alcan Centre de Recherches de Voreppe, BP 27, 38341 Voreppe Cedex, France*

Received 13 March 2009; received in revised form 21 April 2009; accepted 24 April 2009
Available online 28 May 2009

Abstract

Toughness anisotropy of AA2139 (Al–Cu–Mg) in T351 and T8 conditions has been studied via mechanical testing of smooth and notched specimens of different geometries, loaded in the rolling direction (L) or in the transverse direction (T). Fracture mechanisms were investigated via scanning electron microscopy and synchrotron radiation computed tomography. Contributions to failure anisotropy are identified as: (i) anisotropic initial void shape and growth; (ii) plastic behaviour including isotropic/kinematic hardening and plastic anisotropy; and (iii) nucleation at a second population of second-phase particles leading to coalescence via narrow crack regions. A model based in part on the Gurson–Tvergaard–Needleman approach is constructed to describe and predict deformation behaviour, crack propagation and, in particular, toughness anisotropy. Model parameters are fitted using microstructural data and data on deformation and crack propagation for a range of small test samples. Its transferability has been shown by simulating tests of large M(T) samples.

Keywords: Toughness anisotropy; Aluminium; Synchrotron radiation computed tomography; Gurson model; Kinematic hardening

1. Introduction

Anisotropic mechanical properties are common in plastically deformed or thermomechanically processed metallic materials, e.g. in rolled sheet. One particularly important issue in design is the toughness anisotropy of these materials. Furthermore, the transferability of toughness trends between small test pieces and larger structures is an important aspect in optimizing materials performance in practice. Thus, a validated model linking microstructure and fracture micromechanisms to full-scale component behaviour (e.g. full-scale toughness) will be of great value in optimizing materials performance and in providing predictions of full-scale component behaviour.

Anisotropic plastic behaviour has been the subject of many studies, and a number of models have been proposed at both the microscopic level using a polycrystalline description for the material (e.g. [1]) and at the macroscopic level (e.g. [2]). Studies dealing with anisotropic rupture properties are less numerous, although there are many examples for cases where the fracture resistance of structures made of sheet materials must be qualified, e.g. steel pipelines, aluminium alloys for aircraft fuselage, zirconium alloys for nuclear fuel cladding. Several causes may lie at the origin of anisotropic rupture properties:

(i) Anisotropic plastic properties, usually related to the development of specific crystallographic textures, lead to different mechanical responses in different directions so that the plastic energy dissipated during fracture may be anisotropic [3,4]. In addition, local crack tip stresses and strains may be affected by plasticity and in particular by the shape of the yield function.

* Corresponding author. Address: Mines ParisTech, Centre des matériaux, CNRS UMR 7633, BP87 91003 Evry Cedex, France. Tel.: +33 1 60 76 30 37; fax: +33 1 60 76 31 50.
E-mail address: thilo.morgeneyer@mines-paristech.fr (T.F. Morgeneyer).

1359-6454/$36.00 © 2009 Acta Materialia Inc. Published by Elsevier Ltd. All rights reserved.
doi:10.1016/j.actamat.2009.04.046

Depending on the loading direction, local parameters controlling damage growth (such as stress triaxiality ratio) may depend on the loading direction [5].

(ii) Processing conditions (e.g. hot rolling) may create initially anisotropic defects such as elongated voids and/or inclusions and anisotropic defect distribution which will lead to anisotropic fracture properties as experimentally shown in Refs. [6–10].

(iii) Sheet materials are often prestrained so that they can exhibit anisotropic properties due to kinematic hardening. Recent experimental results have shown that prestrain can affect ductility [11].

Several models incorporating the above-mentioned possible mechanisms for fracture anisotropy have been proposed in the literature. Models are either based on the micromechanical Gurson model [12] and its "standard" extension proposed by Tvergaard and Needleman (the so-called GTN model) [13] or the phenomenological Lemaitre model [14,15]. In the present study, extensions based on the GTN model will be used. Introducing plastic anisotropy can be easily done by replacing the von Mises stress in the expression of yield surface given by the GTN model by any anisotropic stress measure. The Hill [16] equivalent stress approach was first used as in Refs. [3,17,18] but more advanced macroscopic models [2,19,20] recently proposed can also be used as shown in Refs. [4,21]. Models accounting for initial void shape and void shape evolution have been developed for prolate and oblate voids by Gologanu and co-workers [22,23]. The model was further extended to account for void coalescence [8,24–26] based on the initial developments of Thomason [27]. These works have shown that ductility and toughness are increased in the case of elongated cavities with the principal loading direction corresponding to the axis of symmetry due to both the cavity shape which slows down void growth and the increased inter-void ligament which delayed void coalescence. The opposite effect is obtained for flat cavities. The model has, however, a major limitation: cavities are assumed to be and remain axisymmetric so that the model must be adapted for non-axisymmetric mechanical loadings (in practice as soon as the model is used in a finite-element code) [28]. The model was coupled with Hill anisotropy in Ref. [28] to study ductility of an X52 pipeline steel. Models based on the GTN approach that simultaneously account for ductile damage and kinematic hardening have been proposed in the literature, but little verification or testing in comparison with actual experiments has been undertaken [29–31]. Up to now, these models have not been coupled either with plastic anisotropy or with void shape effects. These models account for void growth leading to final failure by internal necking [27] but do not account for coalescence by void sheeting [32]. This phenomenon can, however, be observed in thin sheet materials [33] and should be accounted for.

In this work, an experimental study involving the determination of microstructural parameters, mechanical testing and fractography including novel tomography studies of arrested cracks at high stress triaxiality is presented. Subsequently a new model is suggested that incorporates: (i) anisotropic initial void shape and growth; (ii) plastic behaviour, including isotropic/kinematic hardening and plastic anisotropy; and (iii) nucleation at a second population of second-phase particles leading to coalescence. To the best of our knowledge it is the first model to include these three components. The effect of void shape is accounted for using a novel simplified description which has the advantage of not being restricted to axisymmetric cases. Model parameters are determined using the experimentally obtained data. The model incorporates simple representations of coalescence by internal necking and void sheeting. The model is validated by comparing simulated and experimental load–displacement curves obtained on large M(T) panels [34].

2. Experimental

A 3.2 mm sheet of AA2139-T351 was supplied, i.e. solutionized, 2% stretch and naturally aged (see Table 1 for composition). Testing was carried out on T351 material (for brevity identified here as "T3"), and after additional ageing at 175 °C for 16 h to approximate a T8 condition. The intermetallic content has been measured via grey value thresholding of field emission gun scanning electron microscopy (FEG-SEM) images obtained in backscattered electron mode. Dispersoids have been observed with a FEI Quanta 600 microscope.

In this study four types of specimen have been utilised (see Fig. 1): smooth flat tensile specimens, notched flat tensile specimens (EU2), Kahn tear test specimens, and large M(T) panels. Tests on notched EU2 specimens in particular allow fracture properties to be investigated at increased stress triaxiality. Two orientations of loading in the sheet plane have been investigated for all samples: rolling direction (L) and long transverse direction (T). In Kahn and M(T) specimens loaded in the L direction, cracks will propagate in the T direction; these tests are referred to as L–T, and vice versa for T–L designated tests. At least two tests have been performed in each condition/direction combination, whilst for the M(T) sample only one test has been

Table 1
Composition limits of alloy AA2139 (wt.%).

Si	Fe	Cu	Mn	Mg	Ag	Ti	Zn
$\leqslant$0.1	$\leqslant$0.15	4.5–5.5	0.20–0.6	0.20–0.8	0.15–0.6	$\leqslant$0.15	$\leqslant$0.25

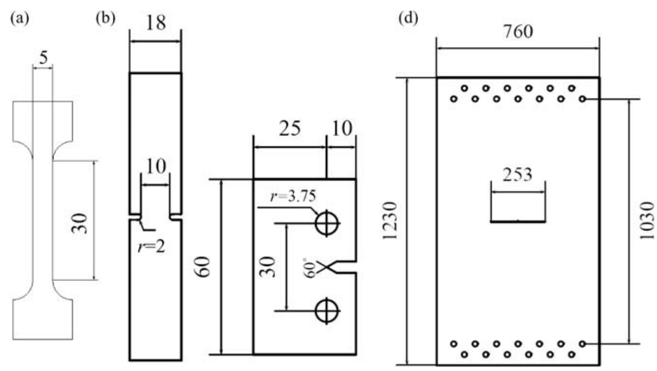

Fig. 1. Specimen geometries for: (a) tensile samples; (b) EU2 samples; (c) Kahn tear test samples; (d) M(T) samples (all dimensions in mm).

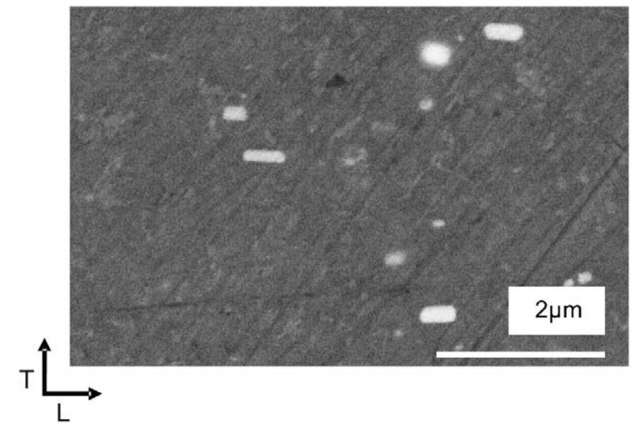

Fig. 2. FEG-SEM image in backscattered mode (20 kV) of in the L–T plane showing dispersoids.

performed per condition/direction. For technical reasons, M(T) tests for T–L loading have only been carried out for the T3 condition. Testing speeds are given in Ref. [21].

The sample preparation for synchrotron radiation computed tomography (SRCT) and SEM has been carried out as described previously [10]. For the analysis of arrested cracks in the initiation region, use was made of custom image data manipulation routines. The cracks are first binarized using a series of morphological operations then analyzed using a "sum along ray algorithm" [35]. The aim was to precisely determine and quantify the local crack characteristics such as opening within the three-dimensional (3-D) volume.

3. Experimental results and analysis

3.1. Material microstructure

Mean anisotropic pore dimensions (3-D Feret measurements) and volume fractions of pores and particles are given in Table 2. Mean Feret dimensions of 3-D Voronoi tessellation [36] of cells around pores and intermetallic particles revealed isotropic distribution of pores and particles.

Some intermetallic particles were, however, seen to be aligned as stringers in the L direction with stringer dimensions of the order of 15–30 μm (cf. 1–10 μm in T and 1–6 μm in the short-transverse direction (S) (see also Ref. [10])). Fig. 2 shows a FEG-SEM image in backscattered mode of the material in the L–T plane. Dispersoids can be seen to be elongated in the L direction.

3.2. Tensile testing on smooth and notched flat specimens

Fig. 3 shows the results of tensile tests on smooth specimens. In the T3 condition (Fig. 3a) tensile behaviour is anisotropic: for testing in the L direction yield strength as well as loads for the same elongation are higher than for testing in the T direction. The transition between the elastic and plastic part of the deformation curve is smooth for T testing but relatively sharp for L testing. The through-thickness deformation is essentially the same for the two testing directions; the slope of the through-thickness variation vs. applied strain is close to 0.5 as for isotropic behaviour. The slight difference in initial tensile curve shape is likely to be mostly due to the prestraining by ~2% that the material has undergone. For the material in the T8 condition (Fig. 3b) tensile deformation curves in the different loading directions, as well as the corresponding through-thickness deformation curves, are essentially identical.

The results of EU2 testing (curves not presented here for brevity) reveal anisotropy in the load curve for the T3 material only, whilst final failure occurs at similar opening displacements. Consistent with the tensile tests, the L and T loading of EU2 samples in the T8 condition do not show significantly different plastic behaviour.

Table 2
Porosity and intermetallic particle content, dimensions and distribution of the AA2139 alloy (pore content and pore Feret dimension were reported previously [10]).

	Porosity			Intermetallic particles		
f_v in (%)	0.34 With a variation of ±10% when setting extreme grey values			0.45 ±15% (standard error based on repeat measurements at different locations and magnifications)		
	Mean Feret dimensions of pores in μm			Mean Feret dimensions of Voronoi cells around 2nd phase particles and pores in μm		
	L	T	S	L	T	S
	7.6	5.4	4.5	23	24	25

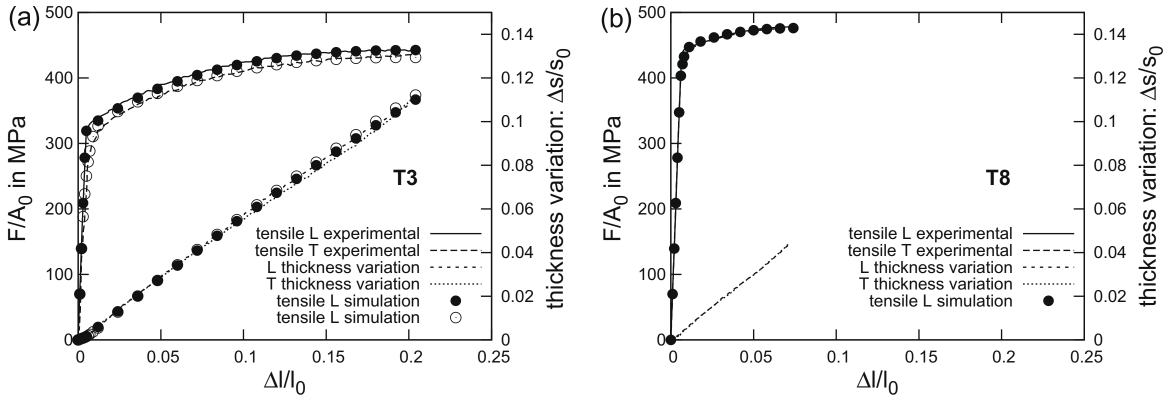

Fig. 3. Tensile tests experimental and simulation for naturally aged and artificially aged (T3 and T8) material.

3.3. Kahn tear testing

Fig. 4 shows the results of the Kahn tear tests [37] in terms of force F divided by the initial ligament area A_0 as a function of the crack mouth opening displacement (CMOD) along with the crack length as a function of the CMOD for L–T and T–L testing for the T3 and T8 conditions. For the T3 material (Fig. 4a) the nominal load is smaller for the T–L tests as compared to the L–T tests up to maximum loads from ∼100 MPa onwards (i.e. indicating a lower initiation toughness). The load differences between the T–L and L–T tests are even higher in the propagation region and crack growth is faster in the T–L test orientation than in the L–T orientation. The unit initiation energy (UIE, defined as the integral $\int F/A_0 \, dl_d$, where dl_d is the pin displacement, taken from the start of the test to maximum load [7]) for the tests are shown in Table 3. For the T3 condition the UIE for the T–L sample is ∼15% lower than for the L–T sample. For the T8 material (Fig. 4b) the nominal load is very similar for both sample orientations up to the maximum load of the T–L sample. However, as the maximum load of the L–T sample is higher and is reached at increased pin displacement, the UIE is 30% higher for the L–T sample than for the T–L. Nominal stresses in the propagation region are substantially lower for the T–L sample than for the L–T sample and crack growth is faster for the T–L test compared to the L–T.

Table 3
Unit initiation energy (UIE) for Kahn tear tests for the loading directions L–T and T–L and T3 and T8 conditions.

	T3 (N/mm)	T8 (N/mm)
L–T	171	104
T–L	148	79

3.4. M(T) testing

Fig. 5 shows the results of M(T) tests for (a) the T3 condition (T–L loading only) and (b) the T8 condition (for both loading directions). Strong toughness anisotropy can be identified for the T8 material. The maximum load of the L–T sample is ∼24% higher than for the T–L sample, which is clearly higher than the corresponding anisotropy measured for the Kahn tear tests (8%, see Fig. 4).

4. Fractography

4.1. Fractography of Kahn samples

For brevity the fractography images are not presented here but the results are briefly summarized. In the flat triangular region where the crack initiates from the notch [33] coarse voids appear to have mainly coalesced via

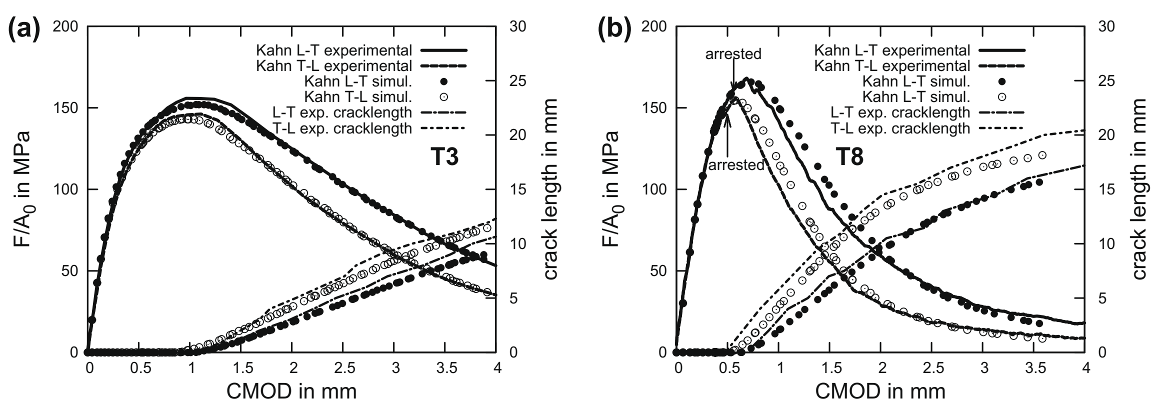

Fig. 4. Kahn tear test tests experimental and simulation for naturally aged and artificially aged (T3 and T8) materials.

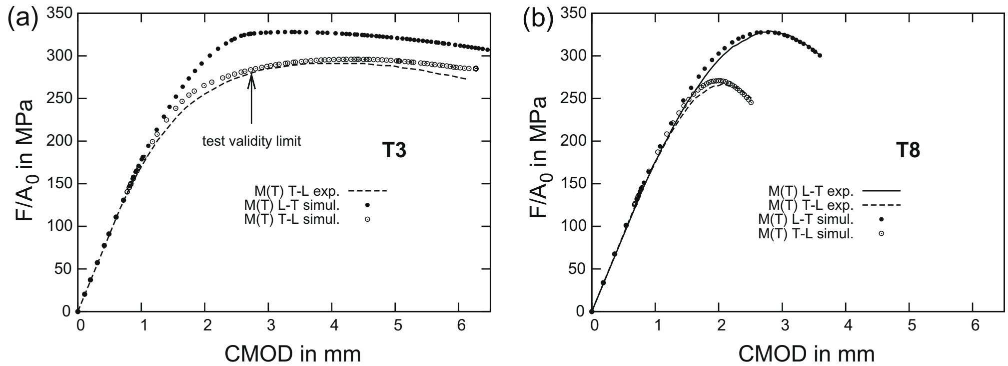

Fig. 5. M(T) test results for simulation and experiment for naturally aged and artificially aged (T3 and T8) materials.

impingement. The dimples are coarser for the T3 condition than for the T8. For the T–L samples the surface morphology is more obviously directional, with void chains apparent on the fracture surface parallel to the material rolling direction.

In the propagation region (the slanted crack growth) at mid-thickness, fracture still seems to be dominated by coarse voiding. However, areas containing fine dimples can also be observed which appear consistent with shear decohesion or also called void sheeting [32]. At the edge of the specimen, the area coverage of microscopically flat regions is higher than at mid-thickness. Fractographic assessment of M(T) sample fracture surfaces has not been carried out here: it has been identified previously that for similar strength Al-alloy sheet, stress states and fracture mechanisms are very similar for Kahn tear test samples and M(T) samples [33].

4.2. SRCT study of fracture initiation in Kahn tear test samples

Tomography scans of arrested cracks allow observation of the initial stages of failure and the subsequent evolution of the fracture process immediately ahead of the crack tip. In the present study the fracture evolution during (flat) crack initiation at high levels of stress triaxiality ahead of the machined notches has been captured in arrested cracks via tomography (also see Fig. 4).

Fig. 6a and b shows a local crack opening map of those cracks for the different loading directions and conditions, as obtained via the sum along ray method [10,35] and 2-D sections normal to the crack propagation direction of cracked scanned volumes (Fig. 6a and b). The locations where the sections are taken from are indicated with lines on the respective COD maps. In all cases there are voids reaching out ahead of the main triangular body of the crack that are often linked to the main crack through narrow (in terms of opening) coalescence regions that may result from nucleation of voids at a second population of small second-phase particles [33]. An especially long void chain reaching ahead the main crack can be seen for the T8 T–L image (see dashed box). Even at this stage of fracture, which is governed by high stress triaxiality that is expected to favour void growth and subsequent coalescence via void impingement [33], clear evidence of coalescence through narrow flat regions is provided in Fig. 6 at the respective crack fronts. Comparison of Fig. 6a with b further shows that coarse voids are larger and more aligned/elongated in crack growth direction in the T8 T–L sample than in the T8 L–T sample, which is consistent with the observation made in T8 T–L and L–T samples of the same material in the propagation region [10]. This results in shorter intervoid ligament distances between for the T–L T8 sample than for the T8 L–T sample.

2-D sections of the crack in the T8 T–L sample are seen in Sections 1 and 2 of Fig. 6c at ~550 and 200 μm from the crack tip, respectively. Abrupt jumps of 100–200 μm are discernible in the cracks in Fig. 6c. The different crack heights are seen to be linked via narrow regions that lie in the sheet plane (see Fig. 6). In the first instance they are thought to lie on grain boundaries as has been identified for an AA6156 alloy [38], but this has not been explicitly confirmed.

Fig. 6d, Sections 1 and 2, show the T8 L–T crack at ~700 and ~300 μm from the crack tip, respectively. Void impingement in columns and shear decohesion that may be the start of slant fracture are discernible. Section 2 of Fig. 6d shows the crack at ~300 μm from the notch tip: at the right part of the crack a narrow region links two coarse voids.

5. Constitutive model

The model aims at representing anisotropic ductile failure of the 2139 aluminium alloy and therefore needs to include the description of the following phenomena: (i) plastic anisotropy, (ii) mixed isotropic/kinematic hardening, (iii) ductile damage by void growth and void sheeting. The model is based on extensions of the GTN model [12,13]. Kinematic hardening is represented by an internal back stress tensor $\underline{X}$. The yield surface is then expressed as a function of $B = \sigma - X$, where σ is the Cauchy stress tensor. Plastic anisotropy is introduced using an anisotropic stress measure B_E defined as [2,20]:

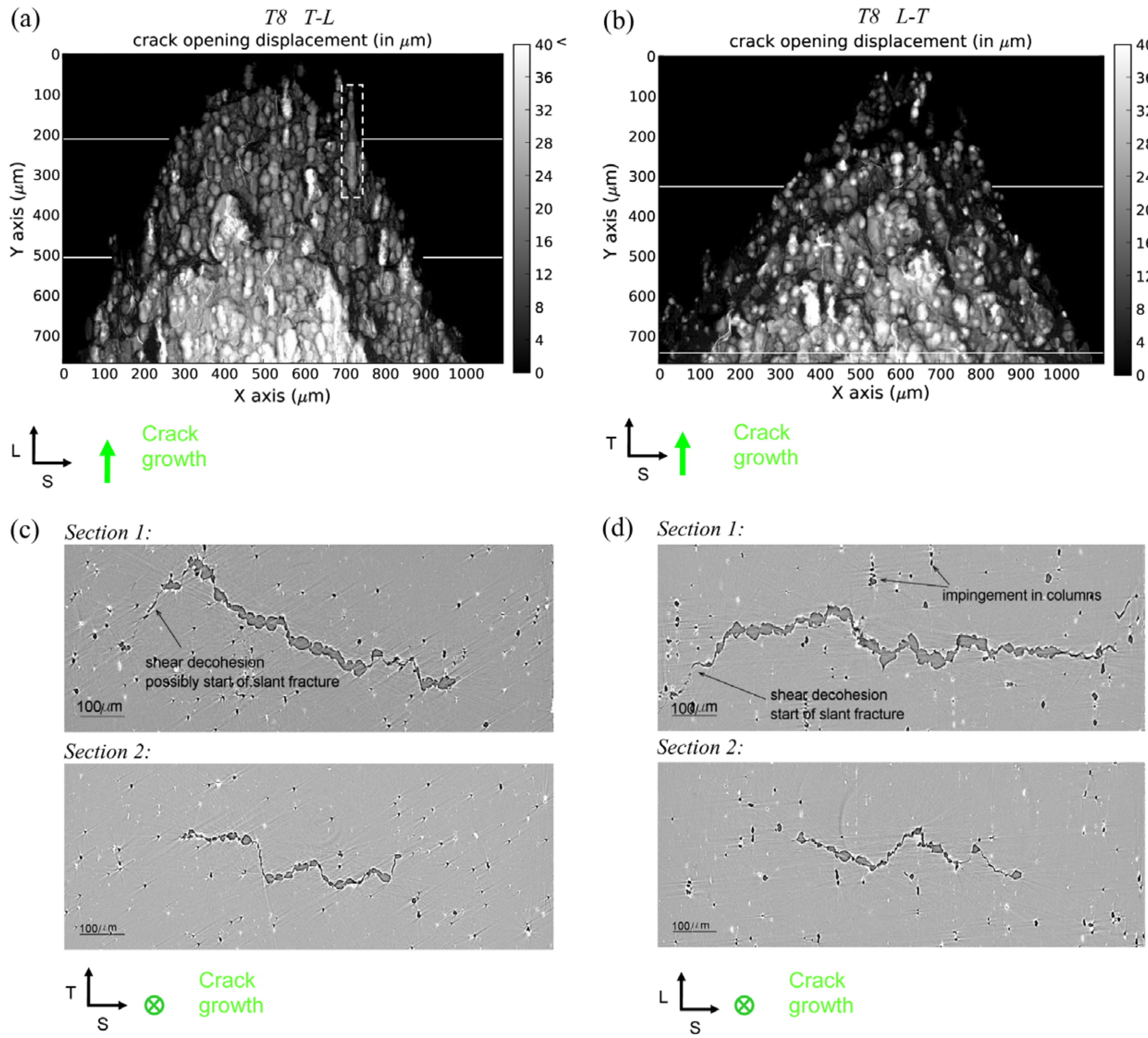

Fig. 6. Representation of the local cack tip opening via a "sum along ray method" for: (a) T–L loading in the T8 condition; (b) L–T loading in the T8 condition (with lines indicating locations of the 2-D sections) and 2-D sections of the SRCT data normal to the crack growth direction; (c) T–L loading in the T8 condition; (d) L–T loading in the T8 condition.

$$B_E = \left(\frac{1}{2}\left(|\tilde{B}_2 - \tilde{B}_3|^b + |\tilde{B}_3 - \tilde{B}_1|^b + |\tilde{B}_1 - \tilde{B}_2|^b\right)\right)^{\frac{1}{b}}, \quad (1)$$

where $\tilde{B}_1 \geq \tilde{B}_2 \geq \tilde{B}_3$ are the eigenvalues of a modified stress deviator $\underline{\tilde{B}} = \underline{\underline{L}} : \underline{B}$ where the fourth-order tensor L is expressed as:

$$\underline{\underline{L}} = \begin{pmatrix} (c^{TT}+c^{SS})/3 & -c^{SS}/3 & -c^{TT}/3 & 0 & 0 & 0 \\ -c^{SS}/3 & (c^{SS}+c^{LL})/3 & -c^{LL}/3 & 0 & 0 & 0 \\ -c^{TT}/3 & -c^{LL}/3 & (c^{LL}+c^{TT})/3 & 0 & 0 & 0 \\ 0 & 0 & 0 & c^{LT} & 0 & 0 \\ 0 & 0 & 0 & 0 & c^{TS} & 0 \\ 0 & 0 & 0 & 0 & 0 & c^{SL} \end{pmatrix}, \quad (2)$$

where $c^{i=LL,\ldots,SL}$ are material coefficients representing plastic anisotropy. Directions L, T and S are assumed to be material directions. Coefficient b represents the shape of the yield function. An isotropic material corresponds to $c^{i=LL,\ldots,SL} = 1$. The usual von Mises yield criterion is then obtained for $b = 2$ or 4. The Tresca yield criterion corresponds to $b = 1$ or $b = +\infty$.

To describe ductile damage, the GTN model is used to define effective scalar stresses [12,13]. Let a be any second-order tensor. The corresponding effective stress, a_*, is implicitly defined by:

$$\Psi(a_*, a_E, a_K, f) = \frac{a_E^2}{a_*^2} + 2q_1 f_* \cosh\left(\frac{q_2}{2}\frac{a_K}{a_*}\right) - 1 - q_1 f_*^2 = 0, \quad (3)$$

where f represents the void volume fraction (porosity). f_* is a function introduced by Tvergaard and Needleman [13] to represent the increased damaging effect of voids during coalescence:

$$f^* = \begin{cases} f_g + f_n & \text{for} \quad f_g < f_c \\ f_c + f_n + \delta(f_g - f_c) & \text{for} \quad f_g > f_c \end{cases}, \quad (4)$$

where f_c represents the critical growth void volume fraction for which coalescence via impingement starts. δ is an "accelerating" factor which represents the increased softening effect of voids once coalescence has started. a_E is the anisotropic stress measure defined by Eq. (1). a_K is introduced to represent in a simplified way 3-D anisotropic void growth and is defined by:

$$a_K = \alpha_{LL} a_{LL} + \alpha_{TT} a_{TT} + \alpha_{SS} a_{SS}, \tag{5}$$

where $\alpha_{i=LL,TT,SS}$ are parameters to be determined. This approximate solution is indeed easier to implement and computationally more efficient than the anisotropic models proposed in Refs. [22,23,25,28] which explicitly account for cavity shape effects. Note that these models are limited to axisymmetric cavities subjected to axisymmetric loading conditions (although they are extended to deal with generic 3-D loadings), whereas the extension proposed here is always valid. The yield function is then constructed using the effective stress associated to $\underline{B}$:

$$\Phi = B_* - R(p), \tag{6}$$

where the function $R(p)$ represents isotropic hardening and p a scalar effective plastic strain. The plastic strain rate tensor is given by the normality rule as:

$$\dot{\underline{\varepsilon}}_p = (1-f)\dot{p}\frac{\partial \Phi}{\partial \underline{\sigma}} = (1-f)\dot{p}\frac{\partial B_*}{\partial \underline{\sigma}} = \dot{p}\underline{n}. \tag{7}$$

It is then necessary to derive evolution laws for the various model variables. The model uses an additive decomposition of the elastic and plastic strain rates so that $\dot{\underline{\varepsilon}} = \dot{\underline{\varepsilon}}_e + \dot{\underline{\varepsilon}}_p$, where $\dot{\underline{\varepsilon}}$ is the strain rate tensor and $\dot{\underline{\varepsilon}}_e$ and $\dot{\underline{\varepsilon}}_p$ are the elastic and plastic strain rate tensors, respectively. The Cauchy stress is computed from the elastic strain tensor using Hooke's law as $\underline{\sigma} = \underline{\underline{E}} : \underline{\varepsilon}_e$, where E is the fourth-order stiffness tensor. Damage growth is controlled by void growth and void nucleation. Accordingly the evolution law for porosity is expressed as [39]:

$$\dot{f} = (1-f)trace(\dot{\underline{\varepsilon}}_p) + (A_n^1 + A_n^2)\dot{p}, \tag{8}$$

where the first term on the right-hand side corresponds to void growth (i.e. mass conservation) and the second term corresponds to void nucleation. Material parameter A_n^1 controls nucleation rate for void nucleation at coarse intermetallic particles. A_n^2 controls nucleation at a second population of smaller second-phase particles observed in slanted areas, which appears to control fracture in low-stress triaxiality regions as evidenced in Ref. [33]. A_n^2 accounts for shear decohesion and void sheeting although slanted crack paths are not simulated (see below). Kinematic hardening is described using an intermediate tensorial variable, α, for which the evolution law is given following the standard expression for non-linear kinematic hardening [40] by:

$$\dot{\underline{\alpha}} = \dot{\underline{\varepsilon}}_p - \frac{3}{2}\frac{D}{C}\dot{p}\underline{X} = \dot{p}\left(\underline{n} - \frac{3}{2}\frac{D}{C}\underline{X}\right), \tag{9}$$

where D and C are two material parameters. The equation used for undamaged materials [40] to relate α and the back stress X (i.e. $\underline{X} = \frac{2}{3}C\underline{\alpha}$) cannot be directly used as the macroscopic back-stress would not vanish as the material breaks (i.e. for $f_* = 1/q_1$). To solve this problem, one defines an intermediate back-stress, χ, which can be interpreted as the back-stress at the microscopic level. χ is related to α using by: $\underline{\chi} = \frac{2}{3}C\underline{\alpha}$. Following Besson and Guillemer-Neel [31], the actual back-stress, X, is computed such that:

$$\underline{\chi} = \frac{2}{3}X_*\frac{\partial X_*}{\partial \underline{X}}. \tag{10}$$

In practice, this equation must be iteratively solved with respect to X. Computing X_* as the solution of $\Psi(X_*, X_E, X_K, f) = 0$ would not give expressions equivalent to that proposed in Ref. [40] for the undamaged material in the limit case $f = 0$ as plastic anisotropy would be taken into account. For that reason, it is preferable to use an isotropic definition of the effective stress to apply the previous equation. In that case, X_* is defined as the solution of $\Psi(X_*, X_{eq}, X_{kk}, f) = 0$ where X_{eq} and X_{kk} are, respectively, the von Mises invariant of X and its trace.

When standard finite-element techniques are used, models including damage lead to material softening and mesh size dependence. In that case, it is necessary to fix the mesh size in order to obtain results transferable from one sample to another [21,41–43] (although improved, so-called "non-local" models can be used to obtain mesh-independent results [44,45]). Consequently, the mesh size, and in particular the mesh height in the direction perpendicular to the crack plane, h [46], should be considered as an adjustable parameter tuned to represent crack growth. It needs to be tuned on specimens containing cracks.

Experiments show that the crack initiates with a flat triangle and propagates in a slant mode of ductile tearing. Simulation of flat to slant transition was performed in Ref. [47] in the case of dynamic crack growth but no attempt was made to compare results with actual tests. The transition was also modelled in Ref. [48] but matching simultaneously crack paths and load–displacement curves was not possible. More recently the flat to slant transition was obtained in Ref. [49,50] but comparison with experiments was also missing. Due to the difficulties en countered to model the transition, the crack is also modelled here as being flat. Material parameters were adjusted to match both load levels and crack lengths. The same solution was adopted in Ref. [21] using the Rousselier model [51] and in Ref. [52] using a 3-D cohesive zone model.

The finite strain formulation is described in Appendix A and the simulation technique is explained in Appendix B.

6. Parameter identification

6.1. Procedure for the naturally aged T351 material

The main material characteristics that are accounted for in the model are: (i) plastic behaviour, consisting of isotropic/kinematic hardening and plastic anisotropy; (ii) void growth; and (iii) nucleation of voids.

For the description of the plastic behaviour the material defects such as initial porosity and void nucleation at coarse second-phase particles needs to be incorporated as volume fractions are high enough for the present material to influence the overall structural behaviour. The fitting of the parameters associated with each of these components is conducted in stages. To fit void growth parameters, unit cell calculations will be used as this has the advantage of providing physical justification to the fitting parameters [53]. In the present identification method the void growth parameters will be fitted before fitting the plastic behaviour using a simplified plastic behaviour that does not account for plastic anisotropy and kinematic hardening. This is justified by the fact that plastic anisotropy is fairly weak and kinematic hardening only influences the material behaviour for strains that are substantially lower than at coalescence. The parameters for void sheeting and nucleation of voids on a smaller population of second-phase particles will be identified for tests on Kahn specimens. An overview over the different steps and parameters of the identification procedure is given in Table 4. The procedure is explained in detail in the following sections.

6.1.1. Identification procedure step 1

2-D axisymmetric unit cell calculations for different stress triaxialities (0.85, 1.00, 1.25, 1.50) have been carried out. The stress triaxialities correspond to values found in finite-element analyses of crack propagation in Kahn tear test specimens. The unit cell is a cylinder with a height of $2H_0$ (oriented in the loading direction) and radius R_0 (see Fig. 7). Periodic boundary conditions are used. The initial porosity is set at 0.34% (determined via microcomputed tomography) and the initial cell aspect ratio H_0/R_0 is set equal to the measured mean Feret dimensions ratios for Voronoi cells around pores and particles, which provides $H_0/R_0 = 1$. To enhance calculation speed, cell calculations

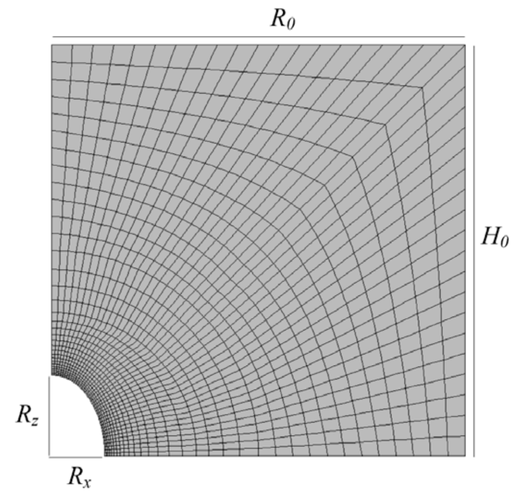

Fig. 7. Example of a 2-D unit cell mesh for loading in the L (vertical) direction. The anisotropic void shape/pore elongation in L can be seen.

were carried out on 2-D meshes. Here for every loading direction (L, T, S) different axisymmetric 2-D meshes are used to account for the average initial pore Feret dimensions in the loading direction obtained from the tomography data of the as-received material. The cavity is assumed to be a different ellipsoid for each loading direction (L, T, S): only the cavity dimension in the direction in which the loads are applied corresponds to the measured average dimension. The other void dimensions are given by the geometrical average of the two other Feret dimensions. For instance, for the case of L-direction loading the void size is given by (see also Fig. 7):

$$\begin{aligned} R_z &= l/2 \\ R_x &= \sqrt{ts}/2 \end{aligned} \tag{11}$$

where l, t, s are the measured initial average pore Feret dimensions of the material (see Table 2) and R_z and R_x

Table 4
Parameter identification procedure for the naturally aged (T3) condition.

Step (1) Void growth parameters: fitting the model to unit cell calculations using an automatic optimization procedure				
Identification of:	Tvergaard Fitting parameter:	q_1		
	Anisotropic void growth parameters:	α_{TT}	α_{LL}	α_{SS}
Step (2) Parameters to fit isotropic/kinematic hardening and plastic anisotropy: (a) Numerical simulation of prestraining by 2% in rolling direction; (b) Simulation of tensile and EU2 tests with initialized parameters and parameter fitting using an automatic optimization procedure				
Identification of:	Isotropic hardening:	R_0	K_1	k_1
	Kinematic hardening:	C	D	
	Plastic anisotropy:	$c^{i=LL,\ldots,SL}$	b	
Step (3) Parameters for nucleation of 2nd population of 2nd phase particles: Trial and error simulation of Kahn tear tests with the aim to fit the nominal stress CMOD curves				
Identification of:	Critical strains for nucleation at 2nd population of 2nd phase particles:	$p_{crit\ L}$	$p_{crit\ T}$	
	Element height:	$h_\perp$		

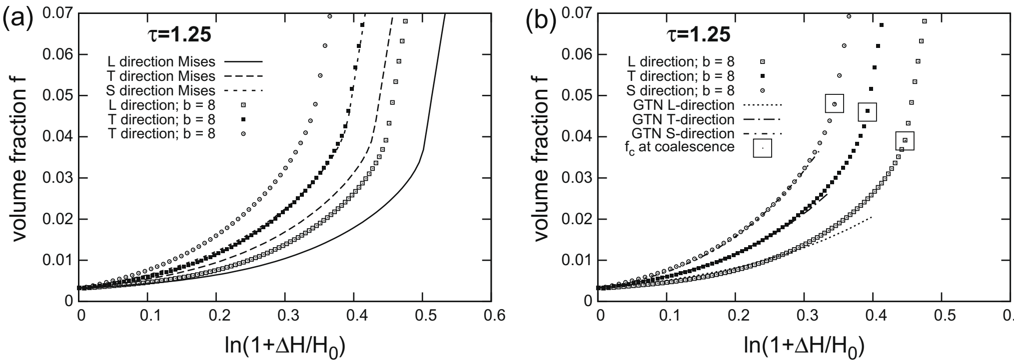

Fig. 8. Results of unit cell calculations for rotation symmetric void cells for different directions at a stress triaxiality of $\tau = 1.25$: (a) comparison of unit cell calculations for $b = 4$ (von Mises) and $b = 8$; (b) comparison of unit cell calculations for $b = 8$ and fitted anisotropic GTN element results (coalescence points are indicated by open square symbols) (alloy in T3 condition; $b = 8$).

are major and minor axis of the pore ellipse. The initial void volume fraction is 0.34% for all calculations. Fig. 8a shows the results of a unit cell calculation in terms of deformation and evolution of void volume fraction for a stress triaxiality of 1.25 for the three loading directions and for different values of b, which is the exponent influencing the yield surface shape as described in Section 5 ($b = 4$ corresponds to the von Mises criterion and $b = 8$ is closer to the Tresca criterion). An initial identification of the parameter b via simulations of EU2 samples and tensile tests on smooth samples neglecting material softening through voids and comparison to experiments lead to $b = 8$. Values higher than 4 are consistent with values given in the literature for Al alloys [2,20]. It can be seen that void growth and coalescence (abrupt slope change corresponds to coalescence) occurs at larger deformation for loading in the L direction than for loading in the T and S directions (Fig. 8a). This trend is consistent with the anisotropic void growth prediction made by the Gologanu–Leblond–Devaux model [22,23]. It can also be seen that the plasticity criterion influences the results substantially: void growth and coalescence occurs faster for the $b = 8$ setting than for the von Mises criterion. The parameter identification is performed using an optimization algorithm and using an elastic–plastic material fitted to L direction tensile test data. Comparison is made for void volume fraction and force evolution. Fig. 8b shows the results of a calculation with a GTN material element using fitted anisotropy parameters for the three different directions. For all subsequent calculations the critical void volume fraction fc is set to 4.5%, which represents an average of the values found in unit cell calculations for different directions and stress triaxilities. The weighting factor δ is set to 3.0. The results of the fitting of the parameters q_1, α_{LL}, α_{TT}, α_{SS} (see also Eq. (5)) are shown in Table 5.

Fig. 9 shows the critical strains at coalescence obtained from unit cell calculations at different stress triaxalities for the L and T loading directions. The difference between critical strain for L and T loading are the higher the lower the stress triaxiality. The higher the stress triaxiality, the lower the strain at coalescence.

Table 5
Parameters for the naturally aged (T3) material simulations.

a) Elastic–plastic behaviour

E in GPa	ν	R_0 in MPa	K_1	k_1
70	0.3	237	1.43	6.90

b) Kinematic hardening

C in MPa	D
14947	261

c) Plastic anisotropy

c^{LL}	c^{TT}	c^{SS}	$c^{i\,=\,LT,TS,SL}$	b
1.1	1.14	0.904	1.0	8

d) Void anisotropy

α_{TT}	α_{LL}	α_{SS}	q_1	f_c	δ
0.967	0.322	1.46	1.81	4.5%	3.0

e) Damage

f_0 *in %*	f_n *in %*	$p_{crit\ L}$ *in %*	$p_{crit\ T}$ *in %*	A_n^{02}
0.34	0.45	35	42	30

f) Element sizes

Height:	Width:	Through-thickness:
100 μm	100 μm	533 μm

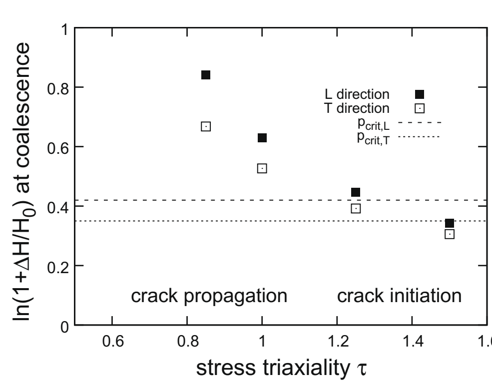

Fig. 9. Results of unit cell calculations of rotation symmetric void cells, critical strains at coalescence for different stress triaxialities and loading in the L and T directions (alloy in T3 condition; $b = 8$).

6.1.2. Identification procedure step 2

To simulate the prestraining, an "imaginary" material, whose properties are supposedly close to the real non-prestrained material, is used which is prestrained in the simulation through loading on a volume element by 2% in the rolling direction L. Subsequently, the prestrained material, whose parameters are initialized during the prestraining, is used to simulate tensile and EU2 tests in the L and T directions. The simulation results are fitted to the experimental results using a simplex optimization algorithm. Parameters for isotropic hardening, kinematic hardening and plastic anisotropy are identified simultaneously in this optimization process. Coefficients $c^{LT,TS,SL}$ play a limited role and are assumed to be equal to 1 as the corresponding shear stresses are close to zero. The following law for the isotropic hardening is used:

$$R(p) = R_0[1 + K_1(1 - e^{-k_1 p})]. \tag{12}$$

The values for void growth parameters (q_1, α_{LL}, α_{TT}, α_{SS}) obtained in step 1 are used. The nucleation of voids on a first population of coarse second-phase particles is taken into account for parameter fitting. Microtomography studies on the material have shown that a certain strain is needed until all coarser second-phase particles are fractured [41]. To represent this effect A_n^1 is expressed as:

$$A_n^1 = \begin{cases} A_n^{01} \ for \quad p_s \leqslant p \leqslant p_e \\ 0 \qquad \text{otherwise} \end{cases}, \tag{13}$$

where A_n^{01} is a constant. Nucleation starts at the beginning of the deformation ($p_s = 0$) and ends at $p_e = 10\%$ strain. This means that the entire volume fraction of coarse second-phase particles (0.4%) is considered to have "transformed" into voids at 10% strain.

6.1.3. Identification procedure step 3

Fig. 10 shows the results of a calculation of Kahn tear tests using the parameters obtained from the first two optimization processes. It can be seen that the anisotropic void growth parameters (α_{LL}, α_{TT}, α_{SS}) do cause a toughness anisotropy in this calculation. It shows that the use of the anisotropic void growth parameters may be an alternative to the Gologanu–Leblond–Devaux model [22,23]. It has been suggested in Ref. [42] that the height of the localization band should be used as the element height. From tomography data it can be seen that the mesh height used (100 μm) may be a reasonable localization band height.

However, the maximum loads as well as the propagation loads are overestimated for a mesh height of 100 μm. As shown in Fig. 10 with an element height of 50 μm, the propagation loads are reduced but still higher than the experimentally found loads. The simulation carried out here does not, however, account for shear decohesion or void sheeting that have been observed experimentally.

In order to be able to fit the descending curve part of the Kahn tear tests it is therefore suggested here to use different critical strains for each loading direction at which the nucleation at a small population of second-phase particles starts. A_n^2 controls nucleation of voids at a second population of smaller second-phase particles leading to coalescence. For the L and T directions different critical strains ($p_{crit\ L}$, $p_{crit\ T}$) are used:

$$A_n^2 = \begin{cases} A_n^{02} \ for \quad p_{criti} \leqslant p \\ 0 \qquad \text{otherwise} \end{cases}, \tag{14}$$

A_n^{02} has high values so that the material is almost immediately breaking when the critical strains are reached.

Using different critical strains is a simplified method to represent damage and coalescence anisotropy and may, for example, be justified by an anisotropic distribution and the shape of small second-phase particles, such as dispersoids (see Fig. 2).

The final parameters found in the optimization and other measured parameters are given in Table 5. They provide mostly excellent fits to the data (see the next section).

6.2. Procedure for the artificially aged (T8) material

The parameter identification for the artificially aged T8 material has been carried out similarly to the naturally aged material (see Table 6). However, as the artificially aged material hardly exhibited any effect of kinematic hardening and plastic anisotropy, these features will not be accounted for in the model. For this reason no prestraining is simulated.

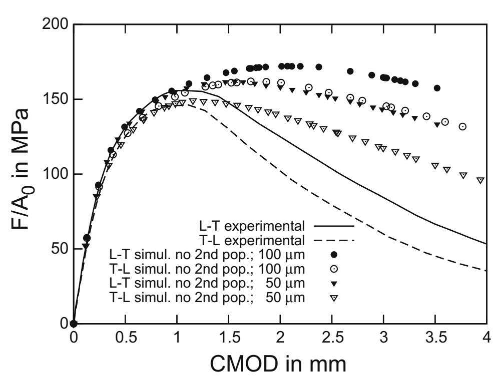

Fig. 10. Simulation of the Kahn tear tests (for alloy in T3 condition) without second nucleation for different mesh sizes (100 and 50 μm element height).

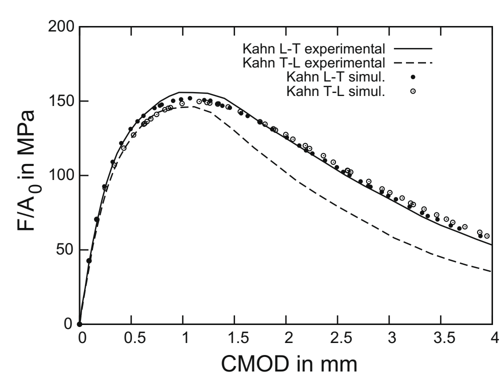

Fig. 11. Simulation of the Kahn tear tests for $p_{crit\ L} = p_{crit\ T} = 42\%$ (T3 condition).

Table 6
Parameters for simulations of the artificially aged (T8) material.

a) Elastic–plastic behaviour							
E in GPa	ν	R_0 in MPa	K_0	K_1	k_1	K_2	k_2
70	0.3	400	0.00832	0.261	16.8	0.115	704
b) Plastic flow			$b = 12$				
c) Void anisotropy							
α_{TT}	α_{LL}	α_{SS}	q_1	f_c	δ		
1.015	0.518	1.317	2.2	4.5%	3.0		
d) Damage							
f_0	f_n	$p_{crit\ L}$	$p_{crit\ T}$	A_n^{02}			
0.34%	0.45%	25%	31%	30.0			
e) Element sizes							
Height:	Width:	Through-thickness					
100 μm	100 μm	533 μm					

It has been found that a good EU2 curve fit can only be obtained for $b = 12$ (close to the Tresca criterion). For $b = 4$ (the von Mises criterion) the loads were too high. The following equation is used for isotropic hardening:

$$R(p) = R_0[1 + K_0 p + K_1(1 - e^{-k_1 p}) + K_2(1 - e^{-k_2 p})]. \qquad (15)$$

The parameters used for the artificially aged material simulations are shown in Table 6.

7. Model predictions

The simulation results for tests on small samples with the fitted parameters are shown here. Using these parameters simulations for tests on large M(T) samples were subsequently performed.

7.1. Comparison with data for small specimens and M(T) specimens

Figs. 3 and 4 show the simulation and experimental results for tensile and Kahn tear testing for the two testing directions and the different heat treatment conditions. A good fit is achieved for the tensile curves (see Fig. 3). The EU2 curves (not presented here) are well predicted for most of the test, but the samples break earlier in the simulations as compared to the experiments, a discrepancy that may be due to the fitting of fracture parameters at higher stress triaxility. The Kahn tear test curves (Fig. 4) are well fitted for the T–L naturally aged and T–L artificially aged materials. The loads obtained from the M(T) simulation of the naturally aged T–L sample are only slightly above the experimental results (see Fig. 5a). The overall prediction is good. Whilst the artificially aged T–L sample loads are slightly overestimated in the simulation, the maximum load ratio between L–T and T–L testing is well represented. The good results of the simulations carried out for M(T) samples (see Fig. 5) provide an independent validation of the model's predictive capabilities (this data has not been used for parameter identification), and thus shows that this method of accounting for toughness anisotropy may represent toughness anisotropy on samples of very different sizes.

7.2. Parametric study on the naturally aged (T3) material: study with the same critical strain (for pcrit L = pcrit T) for both loading configurations

Fig. 11 shows a simulation for the naturally aged material where the same critical strains for the T–L and L–T directions are applied for the second-stage nucleation of voids at small particles. It can be seen that only the first part of the curves is slightly different due to the kinematic hardening and plastic anisotropy. This is consistent with the idea that in this part of the loading the material behaviour is mainly governed by plastic properties. It can be seen that from maximum load onwards the two curves almost superpose. This implies that neither kinematic hardening nor plastic anisotropy are the main cause of the toughness anisotropy. This simulation also shows that the anisotropic growth parameters ($\alpha_{LL,}$ $\alpha_{TT,}$ α_{SS}) have a minor effect in this simulation, and that they cannot explain the toughness anisotropy. Unit cell calculations show that coalescence through impingement occurs at substantially higher strains than the strains (p_c) at which the second-stage nucleation of voids starts, especially at lower stress triaxialities, so that the influence of the anisotropic void growth parameters ($\alpha_{LL,}$ $\alpha_{TT,}$ α_{SS}) is reduced through this second-stage nucleation of voids (also see Fig. 9).

8. Discussion

In a previous finite-element study Pardoen and Hutchison [26] have linked anisotropic shape of initial voids to fracture toughness anisotropy (J_{IC}). In Ref. [10] a comparison between these results and the results on the AA2139 alloy in T8 condition has been made in terms of initial void aspect ratio and toughness anisotropy, in terms of unit initiation energies, at a high level of stress triaxiality. Despite the model simplifications a similar trend in toughness anisotropy has been found for similar initial void volume fractions, consistent with the initial anisotropic void shape controlling the fracture toughness anisotropy.

The present SRCT results provide new insights into fracture mechanisms in the crack initiation region at high stress triaxiality, indicating that coalescence mechanisms involving nucleation at a second population of small second-phase particles may play a role in this stress state. The model presented here can reproduce a similar influence of anisotropic initial void shape on fracture toughness anisotropy as the model of Pardoen and Hutchinson [26] when neglecting nucleation at small particles. However, it is found that for reproducing actual (absolute) toughness values and the load evolution at lower levels of stress triaxiality, an anisotropic nucleation process at the small second-phase particle population must be included in the model. Thus the present modelling indicates that initial void shape anisotropy may not be the only reason for toughness anisotropy and that anisotropic coalescence mechanisms involving a small population of second-phase particles, such as dispersoids [54,55], that display anisotropic morphologies and distributions (see Fig. 2) could substantially contribute to toughness anisotropy. The necessity to introduce different nucleation strains for different directions may also be linked to the distribution of initial porosity and coarse intermetallic particles: the measurement of the mean aspect ratio of Feret dimensions of Voronoi cells around particles and pores provided a value close to one for our material. However, stringers of pores and second-phase particles were observed (see Section 3.1). The heterogeneous distribution of pores and particles may be at the origin of the apparently average isotropic pore and particle distribution measurement. It has been identified that clustering and alignment of pores and particles in the crack propagation region [7,56] can reduce toughness, and TL orientation tests in the present work clearly showed preferential crack advance along individual particle chains ("tongues" appearing at the crack front, as shown in Fig. 6a and b, and also in Ref. [10]). For a better understanding of ductile fracture anisotropy, additional experimental investigation and modelling of pore and particle stringers, and the corresponding percolation of damage though such a heterogeneous structure, may be expected to provide valuable future insights. It is also worth noting that modelling of slant fracture has not been attempted in the present study and the use of the Lode parameter as suggested in Ref. [49,57] should be considered to address this issue.

9. Conclusions

Mechanical tests on smooth and notched specimens of different sizes have been carried out in two loading directions for T351 and T8 heat-treated materials. The T351 material displays isotropic and kinematic hardening, and some plastic anisotropy also plays a role. The T8 material is plastically isotropic. Fractography of Kahn samples has revealed fracture mechanisms linked to coarse voiding and shear decohesion, especially in the propagation region. Some alignment of dimple stringers is prevalent on the T–L sample fracture surfaces in the rolling direction. SRCT studies of arrested cracks in the crack initiation region have revealed the unexpected presence of coalescence through narrow regions that can be linked to void nucleation at a small population of second-phase particles. Anisotropic initial void shape has been identified through SRCT studies of the as-received material. No significant anisotropic average distribution of pores and particles could be measured using Feret dimensions around Voronoi cells. Dispersoid particles are elongated in the L direction of the material.

A model based on the GTN approach has been developed incorporating: (i) anisotropic initial void shape and growth; (ii) plastic behaviour, including isotropic/kinematic hardening and plastic anisotropy; and (iii) nucleation at a second population of second-phase particles leading to coalescence via narrow crack regions.

For the first time a model for kinematic hardening accounting for ductile damage has been successfully applied. A new simple method to account for initially anisotropic void shape and growth is suggested that is easier to implement than other approaches and is not restricted to axisymmetric cavities. Parameters have been fitted on mechanical testing results of small samples. It has been found that neither kinematic hardening nor anisotropic void shape can fully describe the fracture toughness anisotropy. It is proposed to account for coalescence and nucleation at a second population of small second-phase particles via nucleation at different critical strains for the different material directions which may be linked to the anisotropic shape and/or distribution of small second-phase particles such as dispersoids.

Simulation of fracture of large M(T) samples using parameters obtained by fitting on small sample tests shows the good predictive capabilities of the model; the fracture toughness anisotropy on these M(T) panels is correctly predicted. The effect of prestrain and plastic anisotropy is relatively weak for the present material. However, it may be important to use these model features to describe the behaviour of other materials (e.g. steel X100).

Acknowledgements

The authors would like to acknowledge Alcan CRV for financial support and material supply, and Frédéric Bron and Bernard Bès for technical discussion.

Appendix A. Finite-strain formulation

Ductile rupture is always accompanied by large deformations so that a finite-strain formalism must be used when implementing constitutive equations. Specific implementations using the finite strain formalism proposed by Simo [58] and Simo and Miehe [59] have been used by Mahnken [60] and Reusch et al. [61]. A computationally more efficient treatment of finite strain may be obtained using generic formulations based on reference frames which facilitate keeping the standard small strain formulation, i.e. using an additive strain decomposition ($\underline{\dot{\varepsilon}} = \underline{\dot{\varepsilon}}_e + \underline{\dot{\varepsilon}}_p$) [62]. Invariant stress and strain rate measures s and $\underline{\dot{\varepsilon}}$ are defined by transport of the Cauchy stress σ and the deformation rate tensor rate D into the co-rotational reference frame which is characterized by the rotation $\underline{Q}_c : \underline{s} = \underline{Q}_c \cdot \underline{\sigma} \cdot \underline{Q}_c^T$ and $\underline{\dot{\varepsilon}} = \underline{Q}_c \cdot \underline{D} \cdot \underline{Q}_c^T$. The evolution law for Q_c is expressed as:

$$\underline{\dot{Q}}_c = \underline{\Omega}.\underline{Q}_c \text{ with } \underline{\dot{Q}}_c(t=0) = \underline{1}, \tag{16}$$

where $\underline{D}$ and $\underline{\Omega}$ are, respectively, the symmetric and the skew-symmetric parts of the velocity field gradient. The corresponding objective stress rate is the Jaumann rate.

Appendix B. Simulation technique

The modified GTN model was implemented in the finite-element software Zebulon, developed at Ecole des Mines de Paris [63,64]. Similar meshes as in Ref. [21] have been used. An implicit scheme is used to integrate the constitutive equations. The consistent tangent matrix is computed using the method proposed in Ref. [65]. The material is considered as broken when f_* reaches $1/q_1$. In that case, the material behaviour is replaced by an elastic behaviour with a very low stiffness (Young's modulus: $E_b = 1$ MPa). A similar technique was used in Ref. [63] showing convergence of the results for sufficiently low values of the Young's modulus E_b. Gauss points where these conditions are met are referred to as "broken Gauss points". Calculations were done using 3-D brick linear elements with full integration using a B-bar method to control volume change in each element [66]. When all Gauss points in an element are "broken", the element is removed from the calculation. Convergence in terms of macroscopic load and local damage growth was checked as proposed in Ref. [59]. Usual symmetry conditions are accounted for in order to reduce the size of the calculations.

References

[1] Cailletaud G. Int J Plasticity 1992;8:55–73.
[2] Bron F, Besson J. Int J Plasticity 2004;20:937–63.
[3] Rivalin F, Besson J, Pineau A, Di Fant M. Eng Fract Mech 2000;68:347–64.
[4] Tanguy B, Luu TT, Perrin G, Pineau A, Besson J. Int J Press Vess Pip 2008;85:322–35.
[5] Benzerga A, Besson J, Batisse R, Pineau A. Modell Sim Mater Sci Eng 2002;10:73–102.
[6] Steglich D, Brocks W, Heerens J, Pardoen T. Eng Fract Mech 2008;75:3692–706.
[7] Dumont D, Deschamps A, Brechet Y. Mater Sci Eng A 2003;A356: 326–36.
[8] Benzerga A, Besson J, Pineau A. J Eng Mater Technol 1999;121: 221–9.
[9] Benzerga AA, Besson J, Pineau A. Acta Mater 2004;52:4623–38.
[10] Morgeneyer TF, Starink MJ, Sinclair I. Acta Mater 2008;56:1671–9.
[11] Enami K. Eng Fract Mech 2005;72:1089–105.
[12] Gurson AL. J Eng Mater Technol 1977;99:2–15.
[13] Tvergaard V, Needleman A. Acta Metall 1984;32:157–69.
[14] Lemaitre J, Desmorat R, Sauzay M. Eur J Mech 2000;19A:187–208.
[15] Hammi Y, Horstemeyer MF. Int J Plasticity 2007;23:1641–78.
[16] Hill R. The mathematical theory of plasticity. Oxford: Clarendon Press; 1950.
[17] Benzerga AA, Besson J. Eur J Mech 2001;20A:397–434.
[18] Brunet M, Morestin F, Walter-Leberre H. J Mater Process Technol 2005;170:457–70.
[19] Karafillis AP, Boyce MC. J Mech Phys Solids 1993;41:1859–86.
[20] Barlat F, Lege DJ, Brem JC. Int J Plasticity 1991;7:693–712.
[21] Bron F, Besson J. Eng Fract Mech 2006;73:1531–52.
[22] Gologanu M, Leblond J, Devaux J. J Mech Phys Solids 1993;41: 1723–54.
[23] Gologanu M, Leblond JB, Devaux J. J Eng Mater Technol 1994;116:290–7.
[24] Gologanu M, Leblond JB, Perrin G, Devaux J. Int J Solids Struct 2001;38:5581–94.
[25] Pardoen T, Hutchinson JW. J Mech Phys Solids 2000;48: 2467–512.
[26] Pardoen T, Hutchinson JW. Acta Mater 2003;51:133–48.
[27] Thomason PF. Acta Metall 1985;33:1079–85.
[28] Benzerga AA, Besson J, Pineau A. Acta Mater 2004;52:4639–50.
[29] Mear ME, Hutchinson JW. Mech Mater 1985;4:395–407.
[30] Ristinmaa M. Mech Mater 1997;26:227–45.
[31] Besson J, Guillemer-Neel C. Mech Mater 2003;35:1–18.
[32] Garrison WM, Moody NR. J Phys Chem Solids 1987;48:1035–74.
[33] Bron F, Besson J, Pineau A. Mater Sci Eng A 2004;A 380:356–64.
[34] ASTM E561-98; 1999.
[35] Toda H, Sinclair I, Buffière J-Y, et al. Philos Mag 2003;83:2429–40.
[36] Yang N, Boselli J, Sinclair I. J Microsc 2001;201:189–200.
[37] ASTM B 871-01; 2001.
[38] Morgeneyer TF, Starink MJ, Wang SC, Sinclair I. Acta Mater 2008;56:2872–84.
[39] Chu C, Needleman A. Eng Mater Technol 1980;102:249–56.
[40] Lemaitre J, Chaboche JL. Mechanics of solid materials. Cambridge: Cambridge University Press; 1990.
[41] Rousselier G. Nucl Eng Des 1987;105:97–111.
[42] Gullerud AS, Gao X, Dodds RH, Haj-Ali R. Eng Fract Mech 2000;66:65–92.
[43] Ruggieri C, Panontin T, Dodds R. Int J Fract 1996;82:67–95.
[44] Enakoutsa K, Leblond JB, Perrin G. Comput Methods Appl Mech Eng 2007;196:1946–57.
[45] Mediavilla J, Peerlings RHJ, Geers MGD. Int J Numer Meth Eng 2006;66:661–88.
[46] Siegmund T, Brocks W. Int J Fract 1999;99:97–116.
[47] Mathur KK, Needleman A, Tvergaard V. J Mech Phys Solids 1996;44:439–59.
[48] Besson J, Brocks W, Chabanet O, Steglich D. Eur J Finite Elem 2001;10:401–15.
[49] Xue L. Int J Solids Struct 2007;44:5163–81.
[50] Xue L, Wierzbicki T. Eng Fract Mech 2007;75:3276–93.
[51] Rousselier G. In: Continuous damage and fracture; 2000. p. 293–303.
[52] Roychowdhury S, Roy YDA, Dodds RH. Eng Fract Mech 2002;69:983–1002.
[53] Faleskog J, Gao X, Shih CF. Int J Fract 1998;89:355–73.
[54] Broek D. Eng Fract Mech 1973;5:55–66.
[55] Van Stone RH, Merchant RH, Low JR. ASTM STP, vol. 556; 1974. p. 93–124.
[56] Decamp K, Bauvineau L, Besson J, Pineau A. Int J Fract 1997;88: 1–18.
[57] Nahshon K, Hutchinson JW. Eur J Mech 2008;27A:1–17.
[58] Simo JC. Comput Method Appl Mech Eng 1992;99:61–112.
[59] Simo JC, Miehe C. Comput Method Appl Mech Eng 1992;98: 41–104.
[60] Mahnken R. Int J Plasticity 1999;15:1111–37.

[61] Reusch F, Svendsen B, Klingbeil D. Eur J Mech 2003;22A:779–92.
[62] Sidoroff F, Dogui A. Int J Solids Struct 2001;38:9569–78.
[63] Besson J, Steglich D, Brocks W. Int J Solids Struct 2001;38: 8259–84.
[64] Besson J, Foerch R. Comput Method Appl Mech Eng 1997;142: 165–87.
[65] Arndt S, Svendsen B, Klingbeil D. Tech Mech 1997;17:323–32.
[66] Hughes TJR. Int J Numer Meth Eng 1980;15:1413–8.